

<https://doi.org/10.1038/s41524-025-01843-8>

# A comprehensive exploration of thermal transport at Cu/diamond interfaces via machine learning potentials

Zhanpeng Sun<sup>1,2,7</sup>, Hutaao Shi<sup>1,2,7</sup>, Yilong Zhu<sup>1,2</sup>, Rui Li<sup>1,2,3,4,5</sup>, Xiang Sun<sup>1,2,3,4,5</sup>, Qijun Wang<sup>1,2,3,4,5</sup>, Zijun Qi<sup>1,2</sup>, Lijie Li<sup>6</sup>, Sheng Liu<sup>1,2,3,5</sup>, Wei Shen<sup>1,2,3,4,5</sup>✉ & Gai Wu<sup>1,2,3,4,5</sup>✉

The fundamental thermal limitation of pure copper impedes progress in high-power devices, which is becoming more critical with advances in power electronics. The Cu/diamond composite becomes a promising candidate for thermal management due to its excellent theoretical thermal conductivity and customizable coefficient of thermal expansion (CTE). Actually, the thermal conductivity of Cu/diamond composite is much lower than its theoretical value, for which a key bottleneck is interfacial thermal transport at the Cu/diamond interface. However, many atomic-level microscopic mechanisms of heat transport at Cu/diamond interfaces remain poorly understood at present. Especially when different interlayer materials are involved, theoretical studies become extremely complex and challenging. In this work, a machine learning potential for comprehensive simulations of thermal transport at Cu/diamond interfaces has been successfully constructed. The effects of key factors, such as interlayer material, temperature, strain, and crystal orientation, on heat transport at Cu/diamond interfaces have been studied. Furthermore, the underlying mechanisms are thoroughly analyzed and discussed. Finally, the insightful strategies are proposed to optimize and enhance the thermal properties of Cu/diamond interfaces. These advancements can lay a foundation and pave the way for further investigations into interfacial thermal transport at Cu/diamond interfaces as well as in other structures containing interlayer materials.

Copper (Cu), a traditional metallic material with high thermal conductivity, has long been widely used in electronic heat dissipation applications. However, as power electronics technology advances towards miniaturization and enhanced performance, the power density of electronic components is rapidly increasing. The heat dissipation capability of traditional pure Cu has nearly reached its limit, which has seriously restricted the development of high-power devices. As a result, achieving efficient heat dissipation in electronic systems has become one of the technical challenges in recent years<sup>1–3</sup>. Diamond is regarded as the most promising heat dissipation material due to its ultrahigh thermal conductivity (exceeding 2000 W·m<sup>-1</sup>·K<sup>-1</sup>)<sup>4,5</sup>. The combination of Cu and diamond not only significantly improves its thermal conductivity but also allows for the adjustment of its CTE<sup>6</sup>. The integration of Cu and diamond has evolved into several technical approaches, with the following four methods being the most mainstream: (1) direct bonding technology for

Cu/diamond interface construction<sup>7</sup>; (2) direct growth of diamond films on copper substrates, or growth of Cu films on diamond substrates<sup>8</sup>; (3) electroplating copper in through-diamond vias (TDVs)<sup>9</sup>; and (4) development of copper-diamond composites (CDCs)<sup>10–12</sup>. These methodologies advance the collaborative utilization of Cu and diamond through distinct dimensions, including interface engineering, heteroepitaxial growth, micro-nano fabrication, and composite material design. However, due to the weak chemical affinity between Cu and diamond, as well as the large difference in their vibrational spectra, the actual thermal conductivity value of Cu/diamond integration is much lower than the theoretical value<sup>13,14</sup>. The Cu/diamond interface plays a decisive role in the thermal performance of Cu/diamond. Despite efforts to improve thermal transport at the Cu/diamond interface through various fabrication processes and the use of different interlayer materials, the actual thermal conductivity remains quite low<sup>15–18</sup>. Therefore, fully understanding the

<sup>1</sup>School of Integrated Circuits, Wuhan University, Wuhan, China. <sup>2</sup>The Institute of Technological Sciences, Wuhan University, Wuhan, China. <sup>3</sup>School of Power and Mechanical Engineering, Wuhan University, Wuhan, China. <sup>4</sup>Wuhan University Shenzhen Research Institute, Shenzhen, China. <sup>5</sup>Huber Key Laboratory of Electronic Manufacturing and Packaging Integration, Wuhan University, Wuhan, China. <sup>6</sup>College of Engineering, Swansea University, Swansea, UK. <sup>7</sup>These authors contributed equally: Zhanpeng Sun, Hutaao Shi. ✉e-mail: [wei\\_shen@whu.edu.cn](mailto:wei_shen@whu.edu.cn); [wugai1988@whu.edu.cn](mailto:wugai1988@whu.edu.cn)

influence and underlying mechanism of various factors on the interfacial thermal transport in Cu/diamond, from the microscopic atomic scale, is of significant importance for guiding the improvement of the actual thermal conductivity of Cu/diamond. These factors include but are not limited to the interlayer materials, temperature, strain, and crystal orientation.

In order to uncover the microscopic mechanisms of interfacial thermal transport between different materials, molecular dynamics (MD) simulations have been extensively utilized<sup>19,20</sup>. However, the traditional potentials face significant challenges in comprehensively exploring the thermal transport at the Cu/diamond interface, especially when involved with different interlayer materials and various working environments. Against the backdrop of ongoing advancements in artificial intelligence technology, machine learning potentials (MLP) based on the training sets generated by the DFT (density functional theory) method are gradually becoming an important tool in the field of materials science due to their excellent calculation speed and DFT-level accuracy<sup>21–24</sup>. MLPs have demonstrated remarkable adaptability in simulating complex systems with multiple elements and varying conditions<sup>25–27</sup>. Therefore, a comprehensive simulation of thermal transport at the Cu/diamond interface can be effectively achieved based on MLPs. Neuroevolution potential (NEP) stands out among many MLPs due to its higher accuracy and lower cost in atomic simulations for heat transfer applications, and can be obtained via GPUMD (Graphics Processing Unit Molecular Dynamics)<sup>28–30</sup>. It is worth noting that the role of electron-phonon (e-ph) coupling in metal/semiconductor ITC is a topic of significant interest and ongoing debate. Some studies suggest that under transient heating conditions, hot electrons in the metal can indirectly participate in heat transfer to the dielectric through coupling with the lattice, potentially influencing the measured ITC values<sup>31–34</sup>. However, numerous investigations indicate that for typical metal/nonmetal systems, the total interfacial thermal resistance is primarily governed by phonon transport processes at the interface. For instance, Lyeo et al. experimentally reassessed the ITC of Pb/diamond interfaces and found values significantly lower than previously reported “anomalously high” results, consistent with predictions from phonon-dominated models<sup>35</sup>. Similarly, Li et al. demonstrated in a Ni/Al<sub>2</sub>O<sub>3</sub> system that the interfacial thermal resistance is still predominantly contributed by phonon mismatch, with the influence of e-ph coupling being relatively minor<sup>36</sup>. Theoretical studies have also shown that e-ph coupling is not the primary factor accounting for the discrepancies between traditional models and experimental observations<sup>37</sup>. Furthermore, it has been pointed out that e-ph coupling may only play a significant role under specific conditions, such as at strongly bonded interfaces<sup>38</sup> or under high pressure<sup>39</sup>. In our study of the Cu/diamond interface, high-pressure conditions are not involved, and there is no special strong chemical bonding between Cu and diamond. While it is undeniable that e-ph coupling may have an impact on interfacial heat conduction, phonon heat conduction plays an even more important role. Therefore, this work focuses on establishing an NEP to gain a deeper understanding of the phonon heat conduction characteristics of the Cu/diamond interface.

In this work, an NEP suitable for the comprehensive simulation of the interfacial heat transfer in Cu/diamond heterostructure has been successfully constructed. The interlayer materials include Cr, Mo, Ti, W, TiC, and WC. Carbon-based materials such as graphene are also highly promising<sup>40–42</sup>, but this work primarily focuses on common metallic materials and their compounds. The effects of interlayer materials, temperature, strain, and crystal orientation on the thermal transport at the Cu/diamond interface have been studied using non-equilibrium molecular dynamics (NEMD) simulations. The results indicate that among different interlayer materials, those that reduce the phonon bridge distance promote thermal transport at the Cu/diamond interface, while materials that increase the phonon bridge distance tend to suppress thermal transport at the Cu/diamond interface. An increase in system temperature and compression along the heat transfer direction promote thermal transport at the Cu/diamond interface. Conversely, a decrease in system temperature and tension along the heat transfer direction tends to suppress interfacial heat transfer in the Cu/diamond heterostructure. Different crystal orientations of

diamond and Cu also have a significant impact on thermal transport at the interface. It is worth noting that the surface roughness of Cu and diamond can influence interfacial thermal transport<sup>43</sup>. This study focuses on the ideal case with atomically smooth interfaces, and the effects of roughness are not considered.

## Results

### Machine learning performance

The composition of the training data and NEP framework diagram are shown in Fig. 1a. The composition of the training data mainly includes two parts: single crystal and heterostructure. Details on the training data and training hyperparameters can be found in the method section. Figure 1b shows the loss functions for energy, force, and virial. It can be observed that after 300,000 iterations, the relevant parameters in both the training and test data have clearly converged. To more clearly assess the accuracy of NEP, Fig. 2c–g compare the NEP-predicted values of energy, force, and virial with the energy, force, and virial values from DFT calculations for both training and test data. The root-mean-square errors (RMSEs) for energy in the training and test data are both 1.5 meV/atom; for force, they are 129.4 meV/Å and 126.4 meV/Å, respectively; and for virial, they are 28.2 meV/atom and 27.8 meV/atom, respectively. Furthermore, Fig. 2d–h show the error distributions for energy, force, and virial predictions. The R<sup>2</sup> values for energy in the training and test data both reach 0.99; for force, they are 0.98; and for virial, they are 0.96. Both the R<sup>2</sup> values and RMSE values indicate a strong consistency between the NEP predictions and DFT calculations.

To assess the accuracy of NEP in describing the crystal structure, the radial distribution function (RDF) calculated by DFT and NEP are compared, as depicted in Fig. 2a. The peak positions and relative intensities predicted by NEP are in high agreement with the results obtained from DFT-based analysis. This demonstrates that the trained NEP performs excellently in describing the crystal structure. In addition to the crystal structure, the accuracy of NEP in describing thermal properties is also crucial for this work. As an important thermal characteristic, phonon dispersion is commonly employed to judge the quality of atomic interaction potentials. Figure 2b displays the phonon dispersions calculated using DFT and NEP. The phonon dispersions of Cu, diamond, Cr, Mo, W, WC, and TiC predicted by NEP exhibit good agreement with the DFT calculation results. The phonon dispersion of Ti predicted by NEP shows some discrepancies with the phonon dispersion calculated by DFT method in the high-frequency regions at the  $\Gamma$  and K points. After inspection, it is confirmed that this performance is not caused by insufficient precision of training data in this work. The work of Song et al. seems to encounter the same issue<sup>26</sup>. However, it is worth noting that the low-frequency region, which mainly contributes to thermal conductivity, shows good agreement, and the frequency range of the phonon dispersion is also consistent. This suggests that the difference between the phonon thermal properties of Ti described by NEP and DFT method is small. Therefore, this discrepancy is considered acceptable in this work.

### Effects of interface materials on thermal transport

Using interlayers to improve interfacial thermal transport in Cu/diamond heterostructure has been one of the most widely recognized solutions. However, the underlying mechanism by which the interlayer influences the interfacial thermal transport in Cu/diamond remains unclear. In order to deeply understand the process of the interlayer affecting thermal transport, Cu/diamond heterostructure and Cu/X/diamond heterostructure models have been constructed, as shown in Fig. 3a (X = Cr, Mo, Ti, W, TiC, and WC). When WC is used as the interlayer, W atoms and C atoms are not on the same plane, which can lead to two possible bonding situations at interface: either Cu bonds with W atoms, or Cu bonds with C atoms. The former structure is defined as Cu/WC/diamond, while the latter structure is defined as Cu/CW/diamond. In this work, the interlayer is considered a part of the Cu/diamond interface and is therefore included within the interface region. Figure 3b displays the z-axis temperature distribution of heterostructures with 8 different interface structures in the NEMD simulation. The

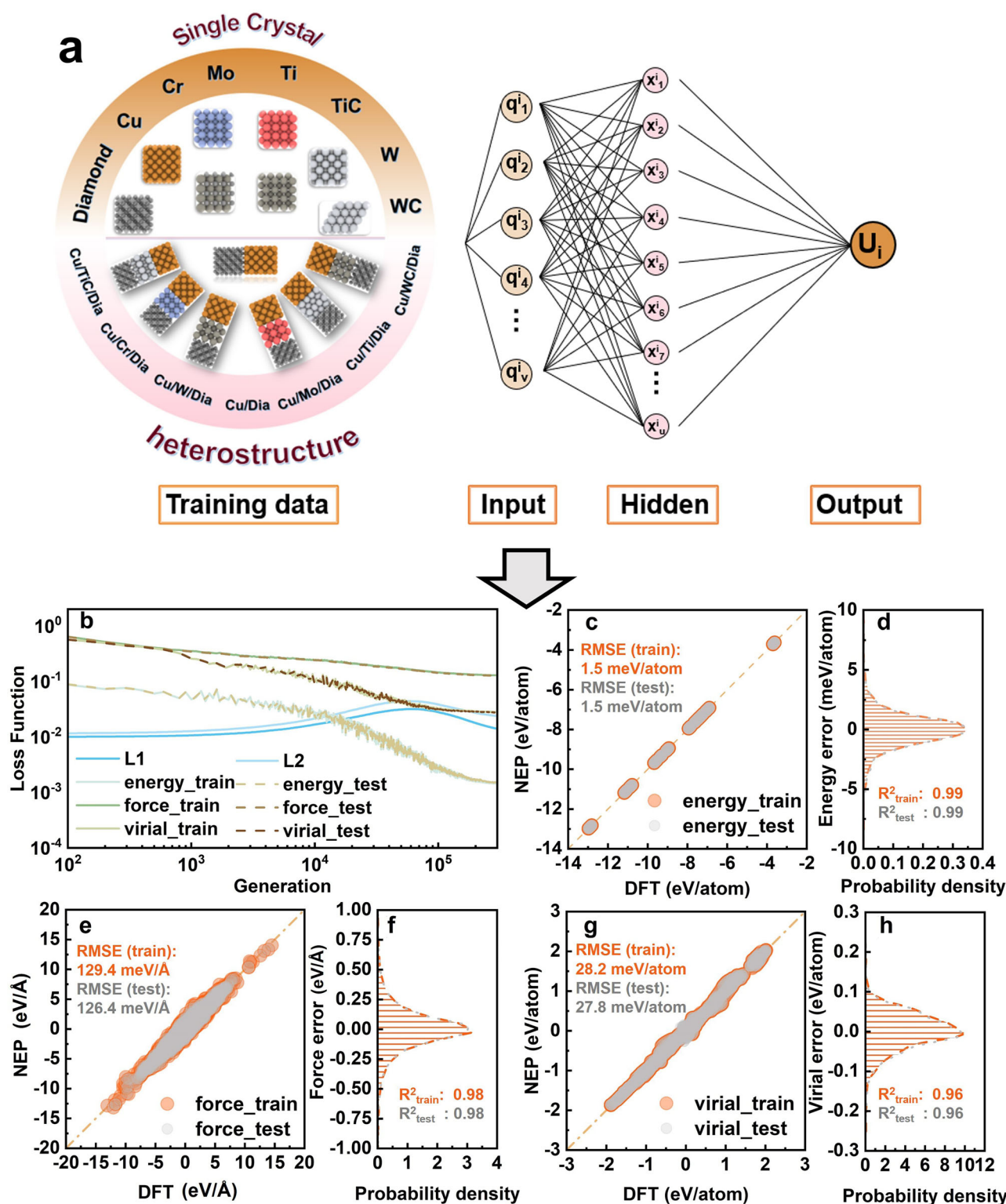


**Fig. 1 | Schematic diagram of NEP framework and performance of machine learning.** **a** Schematic diagram of training data components and NEP framework. **b** Evolution of the loss function during the iteration process. **c, e, g** The comparison

of NEP predicted energy, force and virial values with DFT calculated. **d, f, h** The probability density of energy, force and virial prediction errors.

heat sink and heat source thermostats are set at 275 K and 325 K. The temperature gradient in the Cu region is steeper than that in the diamond region, indicating that the heat dissipation capacity is relatively weak. Different interlayer materials also mainly affect the temperatures of the Cu region. The effect of different interlayer materials on temperature distribution can be clearly observed from the inset in Fig. 3b.

The TBR values at different interfaces are shown in Fig. 3c. When there is no interlayer, the TBR of Cu/diamond is approximately  $10.5 \text{ m}^2 \cdot \text{K} \cdot \text{GW}^{-1}$ . This result aligns well with the value estimated by the DMM theory (approximately  $11 \text{ m}^2 \cdot \text{K} \cdot \text{GW}^{-1}$ <sup>44</sup>). This also further verifies the accuracy of NEP. As shown in Fig. 3c, it can be observed that when Cr, Mo, Ti, and TiC are used as interlayer materials, the thermal transport at the Cu/diamond

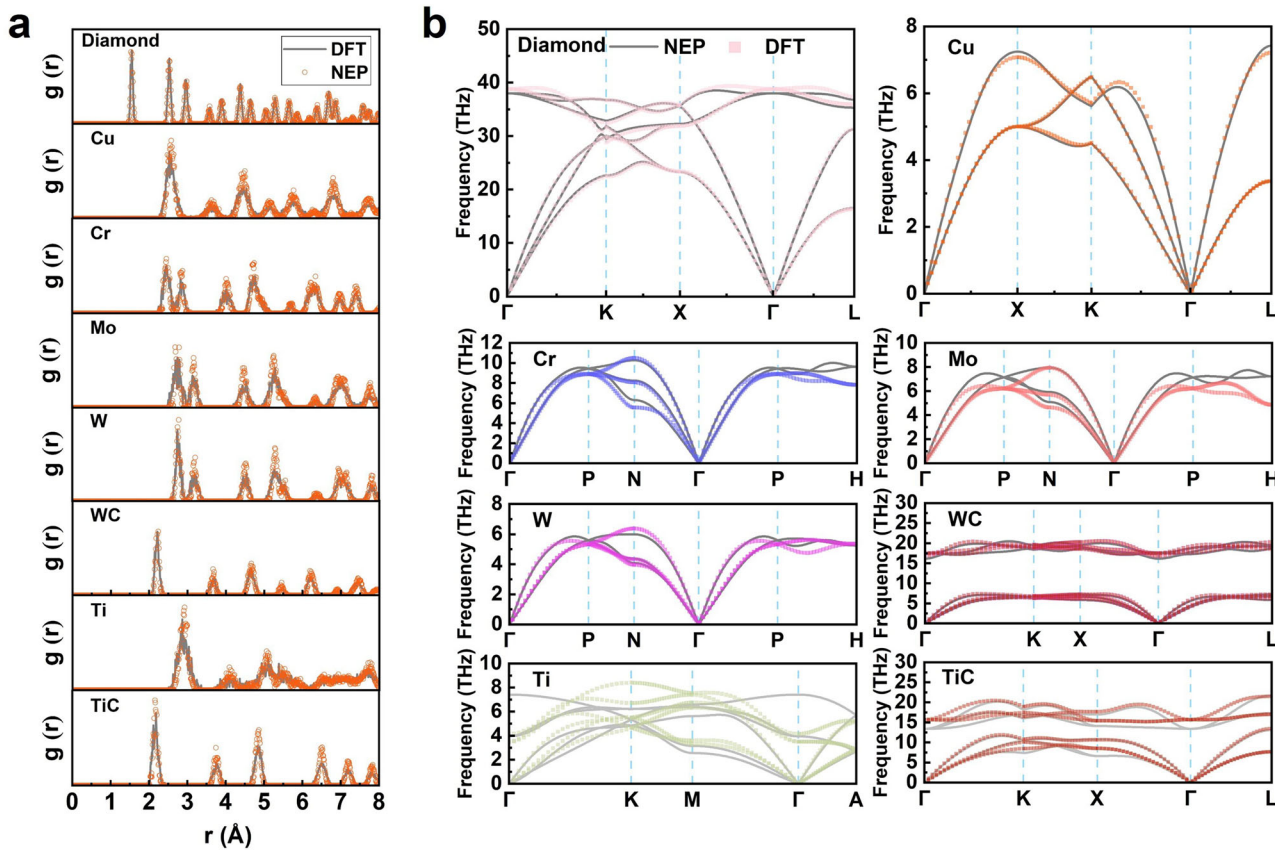


**Fig. 2 | Evaluation of the accuracy of NEP in describing crystal structure and thermal properties.** **a** Comparison of RDF of diamond, Cu, Cr, Mo, W, WC, Ti and TiC calculated by DFT and NEP. **b** Comparison of phonon dispersion of diamond, Cu, Cr, Mo, W, WC, Ti and TiC calculated by DFT and NEP.

interface can be significantly promoted. In particular, when Ti is used as the interlayer material, the TBR can reach  $6.1 \text{ m}^2 \cdot \text{K} \cdot \text{GW}^{-1}$ , which represents a decrease of approximately 42%. When WC is used as the interlayer, its impact on the thermal transport at the Cu/diamond interface is minimal. However, when only W is used as the interlayer material, it significantly hinders the thermal transport at the Cu/diamond interface, and the TBR increases to  $17.4 \text{ m}^2 \cdot \text{K} \cdot \text{GW}^{-1}$ , which represents an increase of approximately 66%.

To further investigate the reasons behind the above phenomenon, the PDOS (phonon density of states) of the single crystal is calculated. In this study, all TBR and PDOS results are computed using GPUMD with NEP as the interatomic potential. Based on this, the vibration spectra of all heterostructures are plotted to allow a clearer observation of the thermal transport at the interface, as shown in Fig. 4. The yellow area represents the high phonon intensity within this frequency range. For the convenience of explanation, it is defined as the efficient phonon channel. The blue area represents the low phonon intensity within this frequency range and it is defined as the inefficient phonon channel. The black area indicates that the phonon intensity in this frequency range is close to or equal to 0, which means that it is difficult for phonons to transport heat in this frequency range. Therefore, it is defined as the phonon wall. It is assumed that phonons tend to transfer heat through the efficient phonon channel. Upon encountering the phonon wall, heat transfer is hindered, and phonons then use the inefficient phonon channels to move to the next efficient phonon channel, as shown in Fig. 4a. The green arrows represent the assumed trajectory of phonon heat transport. The frequency range of the inefficient phonon channel that is used is defined as the phonon bridge, which is represented by a white dashed line in Fig. 4. The length of the phonon bridge at the Cu/diamond interface without an interlayer material is about 26.7 THz. When W is used as the interlayer material, the phonon bridge is lengthened, which means that phonon heat transport

becomes more difficult, as shown in Fig. 4f. This could be an important reason why the TBR at the Cu/diamond interface increases when W is used as the interlayer material. When WC is used as the interlayer material, it can be found that WC has two efficient phonon channels, as shown in Fig. 4g. However, the region close to the efficient phonon channel of diamond cannot connect to the efficient phonon channel of Cu due to the phonon wall. The schematic diagram of phonon heat transfer is shown in the inset of Fig. 4g. Therefore, phonon heat transfer can only occur through the region that connects to the efficient phonon channel of Cu, so the phonon bridge length is approximately 26.7 THz. When using WC as the interlayer material, the phonon bridge length is almost the same as that when no interlayer material is used. This may be the reason why the TBR at the Cu/diamond interface changes minimally when WC is used as the interlayer material. In contrast to the above, when Cr, Mo, Ti and TiC are used as the interlayer materials, the phonon bridges become shorter, resulting in a smaller TBR. It is not difficult to observe that interlayer materials which shorten the phonon bridge length to less than that between Cu and diamond (~26.7 THz) can improve thermal transport at the interface. It can also be found that the TBR at the interface is related to the degree of matching between the efficient phonon channels of the interlayer materials and those of Cu. When Ti is used as the interlayer material, although the phonon bridge is not the shortest, the smallest TBR may result from the good match between the efficient phonon channels of Ti and Cu. When TiC is used as the interlayer material, the phonon bridge length and matching are not excellent enough, but TiC has two efficient phonon channels that can be used for phonon heat transport. The two phonon channels of TiC are connected by abundant inefficient phonon channels, which distinguishes it from WC, as shown in the inset of Fig. 4e. It is this combined heat transfer mechanism that results in excellent thermal transport at interface when TiC is used as the interlayer material. Then, when Cr is used as the interlayer material, its extremely short

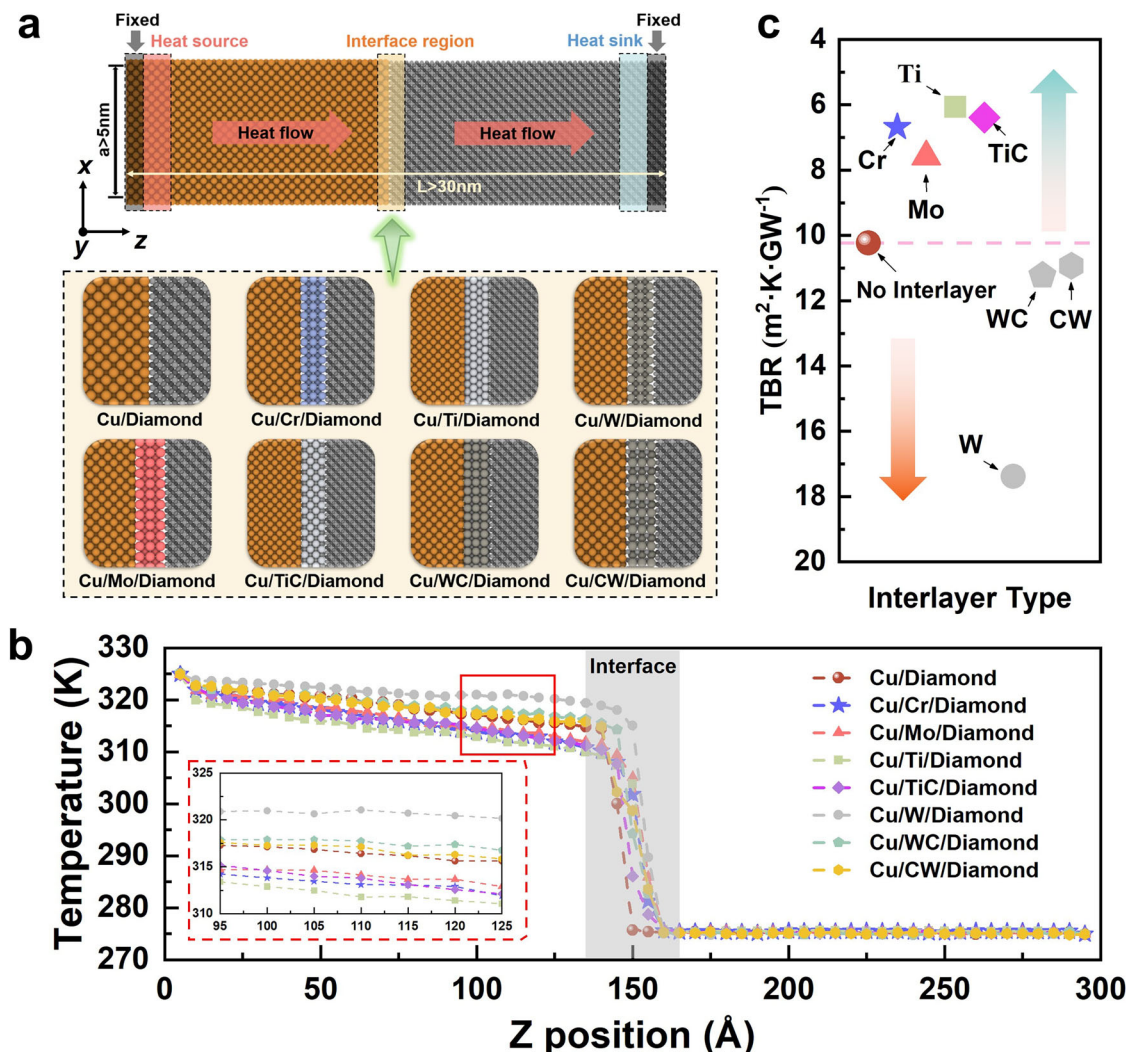


**Fig. 3 | Cu/diamond heterostructure models with different interlayer materials and the corresponding predictions of interfacial heat transfer. a** The Cu/X/diamond heterostructure models. **b** The temperature distribution along the z-axis of the heterostructures with different interlayer materials. **c** The TBR values at different interfaces.

phonon bridge also contributes to a relatively low TBR. The last interlayer material is Mo, and it also leads to a reduction in TBR by approximately 28%.

The interface conductance modal analysis (ICMA) method can help gain a deeper understanding of the contribution of different frequency phonon modes to interfacial thermal conductance (ITC)<sup>45,46</sup>. The contribution of phonon modes at different frequencies to ITC in Cu/X/diamond heterostructures is presented in Fig. 5. From the comparison of Fig. 4a and Fig. 5a, it appears that the 0–10 THz phonon modes contributing to ITC are mainly from Cu, whereas those in the 10–40 THz range are predominantly from diamond. When an interlayer material is introduced (X = Cr, Mo, W, TiC, and WC), the contribution of phonon modes in the 10–25 THz range to ITC is affected, while the contributions from the 0–10 THz and 30–40 THz ranges show minimal variation, as shown in Fig. 5(b, c, and e–h). A different behavior is observed when Ti is employed as the interlayer material, as illustrated in Fig. 5d. As shown in Fig. 4d, the efficient phonon channel of Ti fully overlap with those of Cu and extend slightly beyond the upper limit of Cu. This enables a smooth transition of phonon modes from Cu-dominated contributions in the 0–10 THz range to diamond-dominated ones in the 10–40 THz range. This facilitates more efficient phonon transport from Cu to diamond, which likely contributes to the lower TBR observed when Ti is used as the interlayer material.

In summary, the interfacial thermal transport in Cu/diamond becomes extremely complex after involving the interlayer materials. The method of

the phonon bridge is proposed for intuitive analysis and assessment of the impact of interlayer materials on interface thermal transport. The concept of this method is consistent with the frequency gap law<sup>47</sup>. Furthermore, the effect of all interlayer materials on the phonon heat transport and the contributions of phonon modes at different frequencies to ITC at the Cu/diamond interface are also analyzed in detail. When different interlayer materials are used, an increase in the phonon bridge length results in poorer interfacial thermal transport, whereas a decrease in the phonon bridge length leads to improved thermal transport at the interface. Similar views can also be found in previous work<sup>48</sup>.

#### Effects of temperature on thermal transport

The use of Cu/diamond as a heat sink in high-power devices inevitably encounters temperature variations. Therefore, revealing the impact of temperature on the Cu/diamond interface heat transfer is crucial for understanding the temperature-dependent effects on the thermal properties of Cu/diamond. The thermal transport behavior at the Cu/diamond interface is simulated via the NEMD method in the temperature range of 200 K to 600 K. The temperature distribution along the z-axis is illustrated in Fig. 6a. It can be found that the temperature difference at the interface gradually decreases with the increase of temperature. Similarly, TBR also decreases as the temperature increases, as illustrated in Fig. 6b. Generally, the thermal conductivity of single crystal diamond and Cu decreases as the temperature increases<sup>4,49</sup>. However, the interfacial thermal transport is

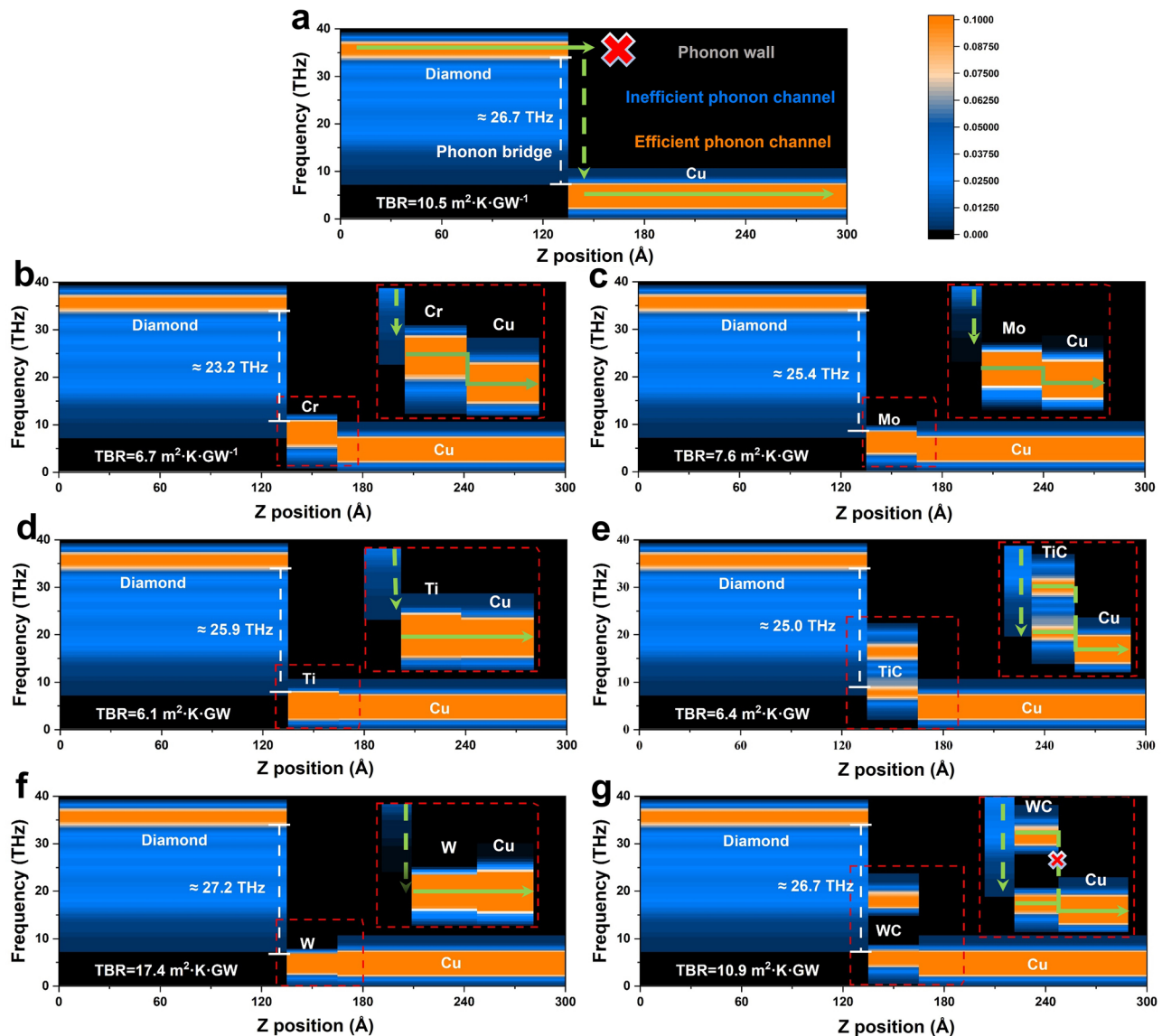


**Fig. 4 |** The vibration spectra of the Cu/diamond heterostructures with different interlayer materials. **a** The vibration spectra of the Cu/diamond heterostructure.

**b** The vibration spectra of the Cu/Cr/diamond heterostructure. **c** The vibration spectra of the Cu/Mo/diamond heterostructure. **d** The vibration spectra of the

Cu/Ti/diamond heterostructure. **e** The vibration spectra of the Cu/TiC/diamond heterostructure. **f** The vibration spectra of the Cu/W/diamond heterostructure. **g** The vibration spectra of the Cu/WC/diamond heterostructure.

enhanced. To further explore the underlying mechanisms, the PDOS of Cu and diamond at various temperatures have been calculated, as illustrated in Fig. 6c. As observed from the inset of Fig. 6c, with increasing temperature, the PDOS of Cu and diamond gradually approach each other, resulting in an increasing overlap ratio of the PDOS, as shown in Fig. 6b. This could be the major reason for the decrease in TBR with the increase of temperature. The above phenomenon suggests that an increase in temperature promotes thermal transport at the Cu/diamond interface, which is a favorable feature for the application of Cu/diamond as a heat dissipation material in high-power devices.

#### Effects of uniaxial strain on thermal transport

Strain engineering is regarded as an effective method to adjust the properties of materials<sup>50,51</sup>. To further improve the heat transfer at the Cu/diamond interface, the effect of uniaxial strain along the heat transfer direction on the TBR is explored. The direction of uniaxial strain application is shown in Fig. 7a, where an  $\epsilon$  value greater than zero denotes tensile strain, and  $\epsilon$  value less than zero indicates compressive strain. As illustrated in Fig. 7b, the TBR increases with the rise in uniaxial tensile strain. Conversely, TBR decreases

as uniaxial compressive strain increases. A strain of  $\pm 3\%$  results in an approximately 114.5% change in TBR, which is quite remarkable. To gain deeper insights into the fundamental reasons behind the effect of strain on TBR, the PDOS of Cu and diamond under different strains are calculated, as illustrated in Fig. 7c. After applying uniaxial tensile strain, the PDOS of Cu and diamond both shift towards the low-frequency region. On the contrary, after applying uniaxial compressive strain, the PDOS of Cu and diamond both shift towards the high-frequency region. Further analysis reveals that the actual strain in the Cu and diamond regions of the heterostructure differs greatly from the overall strain of the heterostructure system due to the significant difference in hardness between Cu and diamond. As shown in Fig. 7d, the actual strain in the Cu region of the heterostructure is greater than the overall strain of the heterostructure system, while the actual strain in the diamond region of the heterostructure is smaller than the overall strain of the system. Moreover, the strain in the Cu and diamond regions of the heterostructure seem to exhibit a linear relationship with the overall strain of the heterostructure system. Therefore, the actual strain in the Cu region of the heterostructure is much greater than that in the diamond region of the heterostructure. The above phenomenon leads to a greater shift

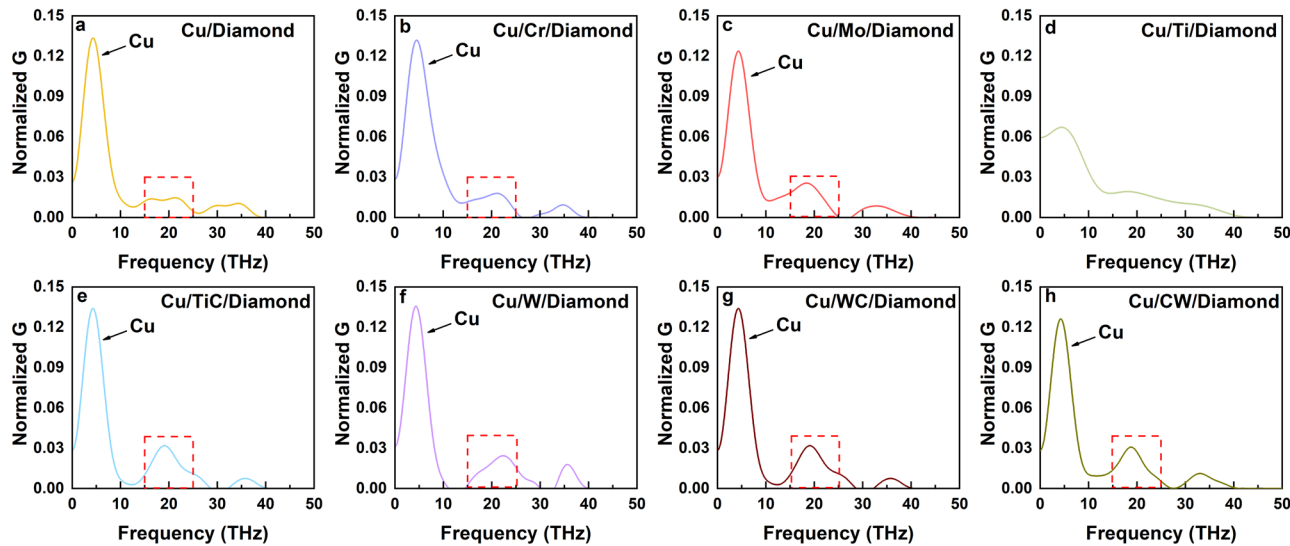
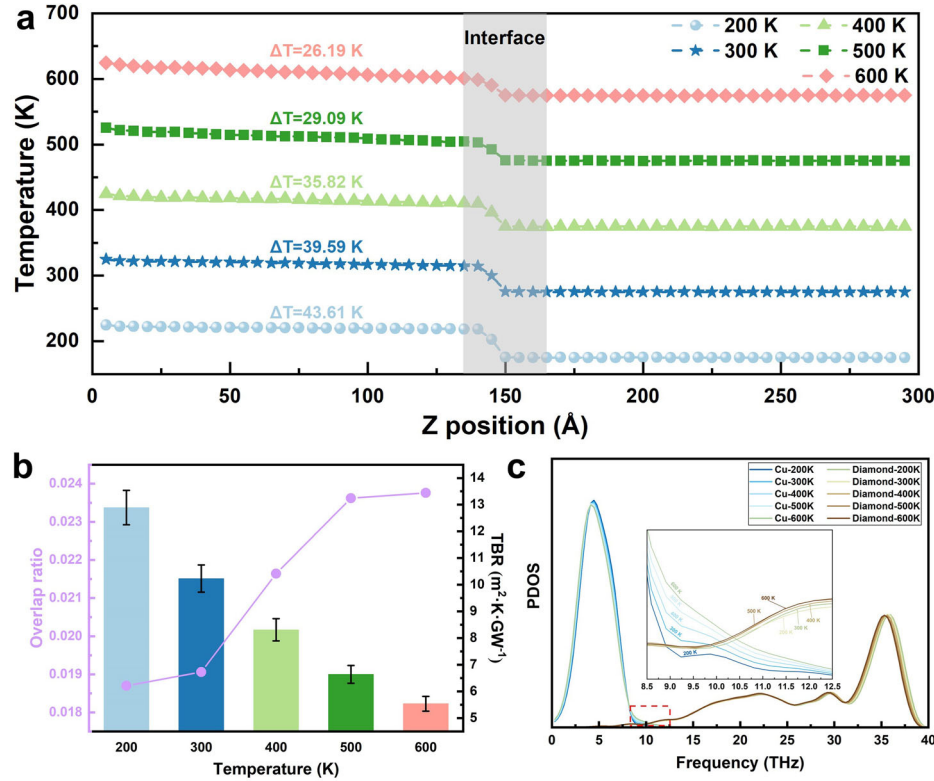


**Fig. 5 | The contribution of phonon modes at different frequencies to ITC in Cu/X/diamond heterostructures.** **a** Cu/diamond heterostructure. **b** Cu/Cr/diamond heterostructure. **c** Cu/Mo/diamond heterostructure. **d** Cu/Ti/diamond

heterostructure. **e** Cu/TiC/diamond heterostructure. **f** Cu/W/diamond heterostructure. **g** Cu/WC/diamond heterostructure. **h** Cu/CW/diamond heterostructure.

**Fig. 6 | Predictions of the effect of temperature on heat transfer.** **a** The temperature distribution along the z-axis of the heterostructures at various temperatures. **b** The TBR and the overlap ratio of PDOS between Cu and diamond at different temperatures. **c** The PDOS of Cu and diamond at various temperatures.

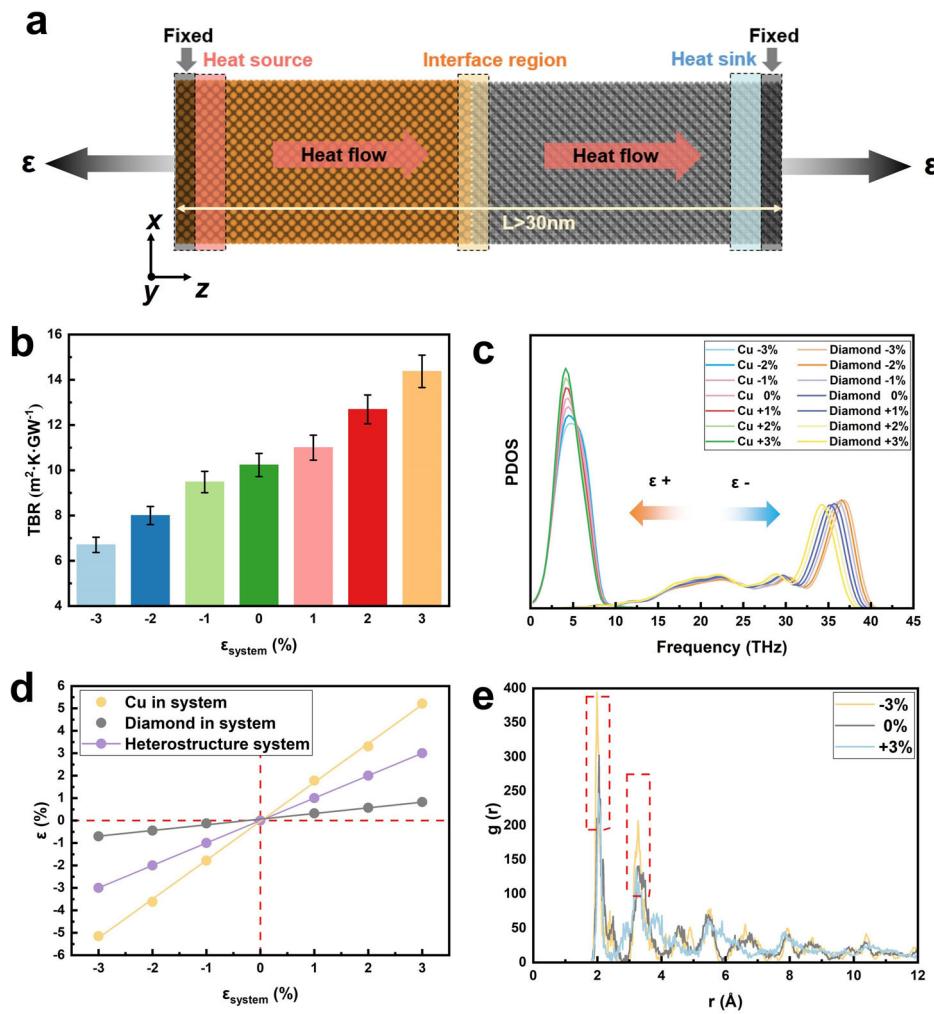


of the PDOS of Cu towards the low-frequency region compared to that of diamond when uniaxial tensile strain is applied to the heterostructure. Similarly, when uniaxial compressive strain is applied to the heterostructure, the PDOS of Cu shifts more toward the high-frequency region than that of diamond. The PDOS of Cu is mainly located in the low-frequency region, while the PDOS of diamond is mainly located in the high-frequency region. This results in a reduced overlap of the PDOS between Cu and diamond when uniaxial tensile strain is applied. Conversely, when uniaxial compressive strain is applied, the overlap between the PDOS of Cu and diamond increases. This may be one of the underlying reasons why the TBR increases

with the increase of uniaxial tensile strain and decreases with the increase of uniaxial compressive strain.

In addition to the overlap of the PDOS, the bonding strength at the interface is also one of the key factors influencing interfacial thermal transport. When uniaxial compressive strain is applied to the heterostructure system, the peak at approximately 2 Å in the RDF of the C and Cu atoms at the interface significantly increases, indicating that more bonds are formed between the C atoms and Cu atoms at the interface. A better bonding strength at the interface also indicates that it is more favorable for thermal transport at the interface. Conversely, when

**Fig. 7 | Schematic diagram of uniaxial strain and predictions of the effect of uniaxial strain on thermal transport.** **a** The schematic diagram of uniaxial strain applied to the Cu/diamond heterostructure, where an  $\epsilon$  value greater than zero denotes tensile strain, and  $\epsilon$  value less than zero indicates compressive strain. **b** The TBR of Cu/diamond interface under different strains. **c** The PDOS of Cu and diamond under different strains. **d** The actual strains corresponding to the internal Cu and diamond regions of the Cu/diamond heterostructure system under different strains. **e** The RDF of C atoms and Cu atoms at the interface under different strains.



uniaxial tensile strain is applied, the peak at approximately 2 Å in the RDF of the C and Cu atoms at the interface decreases, indicating that fewer bonds are formed between the C and Cu atoms at the interface, resulting in a weaker interfacial bonding. This may be another important reason why the TBR increases with the application of uniaxial tensile strain and decreases with the application of uniaxial compressive strain.

In summary, the significant change in TBR at the Cu/diamond interface caused by uniaxial strain is primarily due to the variations in the overlap of the PDOS of Cu and diamond, as well as the changes in bonding strength at the interface. The fundamental reason for the variations in the overlap of the PDOS of Cu and diamond with uniaxial strain is the significant difference in hardness between Cu and diamond. Moreover, the PDOS of Cu with low hardness is primarily located in the low-frequency region, while the PDOS of diamond with high hardness is primarily located in the high-frequency region. This leads to the simultaneous increase in the overlap of PDOS and bonding strength at the interface when uniaxial compressive strain is applied to the heterostructure. On the contrary, when uniaxial tensile strain is applied to the heterostructure, the decrease in the overlap of PDOS and bonding strength at the interface also occurs simultaneously. This is a unique characteristic of the Cu/diamond heterostructure system. On this basis, it can be reasonably inferred that for a heterostructure composed of two materials with similar hardness, or where the PDOS of low-hardness materials is primarily located in the high-frequency region while the PDOS of high-hardness materials is primarily located in the low-frequency region, the regulatory effect of strain on TBR may be weakened.

### Effects of crystal orientation on thermal transport

The crystal orientations of Cu and diamond in Cu/diamond are usually complex<sup>18</sup>. Therefore, revealing the effect of crystal orientation on thermal transport at the Cu/diamond interface is also crucial for understanding the thermal properties of Cu/diamond. In this work, the TBR values of 9 types of heterostructures formed by the (100), (110), and (111) crystal orientations of Cu and diamond are comprehensively predicted, as shown in Fig. 8a, b. The PDOS of Cu and diamond along different crystal orientations is also calculated for further analysis, as shown in Fig. 8c. It can be observed that the PDOS of Cu and diamond along the (100), (110), and (111) crystal orientations is essentially the same. Cu and diamond do not exhibit anisotropy in thermal conductivity, so it is reasonable that the PDOS for the different crystal orientations is consistent, which further validates the accuracy of the NEP in predicting the phonon thermal properties of Cu and diamond. However, the TBR of the heterostructures composed of Cu and diamond with different crystal orientations shows significant differences. This could be related to the inelastic phonon scattering at the interface. In interfacial thermal transport, both elastic phonon scattering and inelastic phonon scattering play significant roles<sup>52,53</sup>. To explore the underlying mechanism of this phenomenon, the ICMA method is employed<sup>45</sup>. The underlying mechanisms behind the influence of crystal orientation on TBR are analyzed using Cu(100)/diamond as a representative heterostructure. The ITC accumulation functions and the contribution of phonon modes at different frequencies to ITC are calculated, as shown in Fig. 8d, e. Here,  $\omega_{\text{max}}$  represents the maximum intrinsic phonon mode frequency of diamond. As can be seen from Fig. 8d, e, the ITC remains unchanged for phonon frequencies above

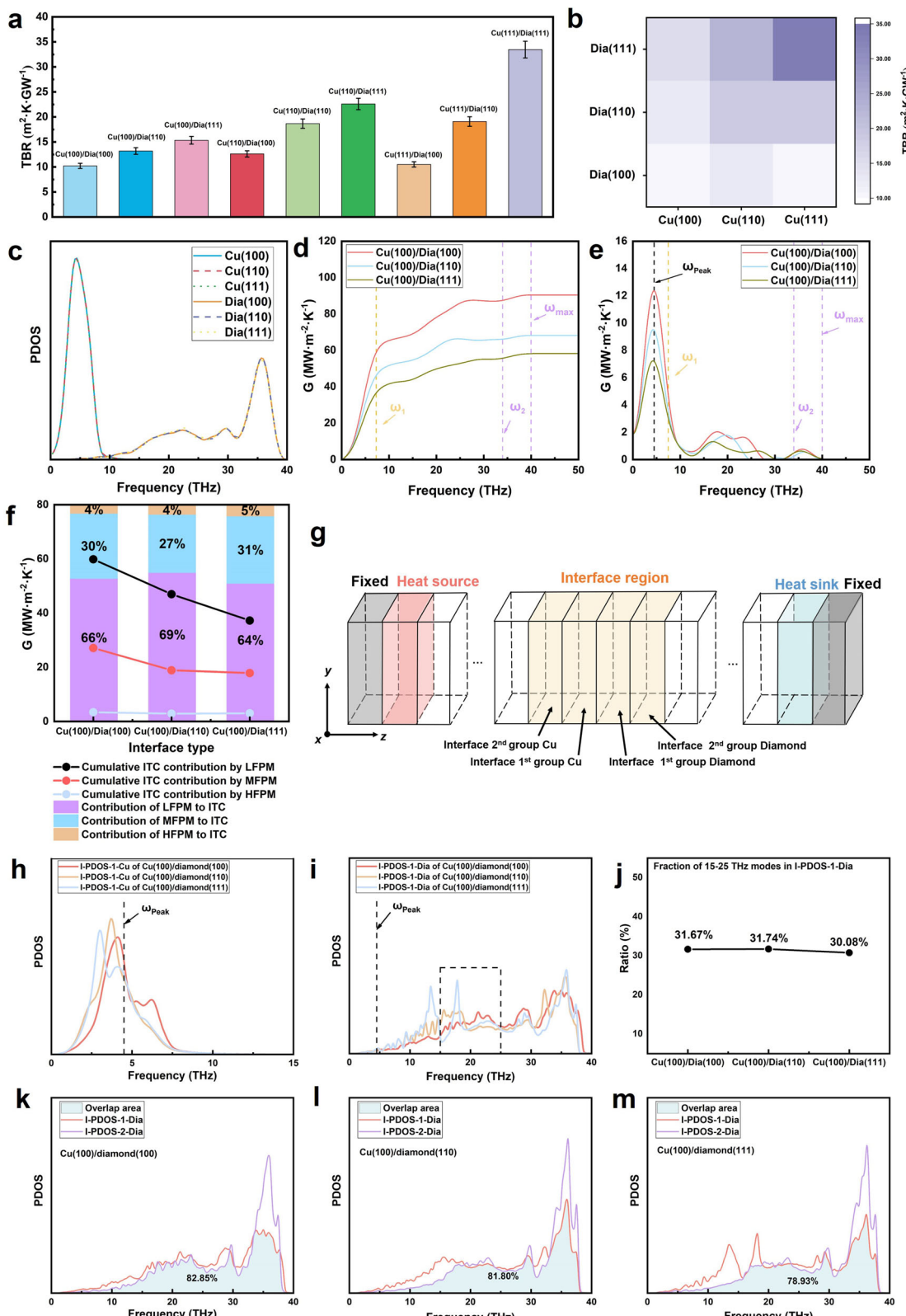


**Fig. 8 | Schematic diagram of interface region components and predictions of the effect of crystal orientation on thermal transport. a, b** The TBR values of 9 types of heterostructures formed by the (100), (110), and (111) crystal orientations of Cu and diamond. **c** The PDOS of Cu and diamond along different crystal orientations. **d** Cumulative functions of ITC with frequency. **e** Contribution of phonon modes at different frequencies to ITC. **f** Cumulative values and contribution percentages of ITC components versus Interface type. **g** Schematic diagram of interface region components. **h** I-PDOS-1 for Cu in the three Cu(100)/diamond heterostructures. **i** I-PDOS-1 for diamond in the three Cu(100)/diamond heterostructures. **j** Fraction of 15–25 THz modes in I-PDOS-1-Dia of Cu(100)/diamond(100), Cu(100)/diamond(110) and Cu(100)/diamond(111) interfaces. **k–m** The overlap of I-PDOS-1 and I-PDOS-2 for diamond in the three Cu(100)/diamond heterostructures.

$\omega_{\max}$  and phonon modes with frequencies higher than  $\omega_{\max}$  contribute negligibly to the ITC, suggesting that no phonon modes above  $\omega_{\max}$  are generated via inelastic phonon scattering. This also suggests that inelastic phonon scattering may occur between the intrinsic phonon frequencies of Cu and diamond. In this work, phonon modes with frequencies below  $\omega_1$  are defined as low-frequency phonon modes (LFPM). Phonon modes with frequencies between  $\omega_1$  and  $\omega_2$  are defined as mid-frequency modes (MFPM). Phonon modes with frequencies between  $\omega_2$  and  $\omega_{\max}$  are defined as high-frequency modes (HFPM). Here,  $\omega_1$  represents the maximum intrinsic phonon mode frequency of Cu,  $\omega_2$  represents the lower frequency limit of the diamond efficient phonon channel, and  $\omega_{\text{peak}}$  represents the phonon mode frequency that contributes most significantly to ITC. The cumulative contributions and contribution percentages of LFPM, MFPM, and HFPM to the ITC are calculated, allowing a clear assessment of the relative importance of different frequency phonon modes in influencing the ITC, as shown in Fig. 8f. As the ITC decreases, the cumulative contribution of LFPM to the ITC declines significantly. The cumulative contribution of MFPM decreases slightly, while the cumulative contribution of HFPM shows no noticeable change. Furthermore, it can be observed that LFPM contributes approximately 65% to the ITC, MFPM contributes about 30%, while HFPM accounts for only around 5%. This suggests that LFPM play an important role in interfacial heat transfer at the Cu/diamond interface. To gain insight into the changes in phonon frequencies at the interface, the interface-PDOS (I-PDOS) is calculated. As shown in Fig. 8g, there are two groups of Cu and two groups of diamond in the interface region in this work. For convenience, the groups of Cu and diamond that are in direct contact are defined as the interface-1<sup>st</sup>-group-Cu and interface-1<sup>st</sup>-group-diamond, and their corresponding PDOS are denoted as I-PDOS-1-Cu and I-PDOS-1-dia. The other groups are defined as the interface-2<sup>nd</sup>-group-Cu and the interface-2<sup>nd</sup>-group-diamond, and their corresponding PDOS are denoted as I-PDOS-2-Cu and I-PDOS-2-dia. The box length of each group in the interface region is defined as 5 Å, which is consistent with the group size used in the NEMD simulations. As shown in Fig. 8h, the peaks of I-PDOS-1-Cu for all three interfaces are located at positions lower than  $\omega_{\text{peak}}$ . Among them, the peak for Cu(100)/diamond(111) exhibits the largest downward shift, followed by Cu(100)/diamond(110), while Cu(100)/diamond(100) shows the smallest shift. LFPM plays an important role in ITC. Therefore, this may be one of the key reasons why the TBR of Cu(100)/diamond(100) is lower than that of Cu(100)/diamond(110), which in turn is lower than that of Cu(100)/diamond(111). A comparison of Fig. 8c and Fig. 8i reveals a notable decrease in the proportion of HFPM and a corresponding increase in MFPM in I-PDOS-1-Dia. This may be caused by inelastic phonon scattering, in which HFPM split into multiple MFPM. The proportion of LFPM shows no significant change. As shown in Fig. 8e, phonon modes in the 10–15 THz range within MFPM make a considerable contribution to ITC. However, unfortunately, the fraction of phonon modes in the 10–15 THz range shows no significant difference among the three interfaces, as shown in Fig. 8j. This may suggest that the inelastic phonon dispersion from HFPM to MFPM does not play a decisive role in enhancing the ITC. Instead, it may suppress elastic phonon heat transport within diamond. As shown in Fig. 8k–m, the overlap percentages between I-PDOS-1-Dia and I-PDOS-2-Dia are 82.85%, 81.80%, and 78.93% for the three interfaces, respectively. A higher overlap percentage may be more favorable for elastic phonon heat transfer within diamond. Therefore, this may be another factor contributing to the lower TBR of Cu(100)/diamond(100) compared to Cu(100)/diamond(110), and that of Cu(100)/diamond(110) compared to Cu(100)/diamond(111).

In summary, the crystal orientations of Cu and diamond have an impact on the thermal transport at the interface. The thermal conductivities of Cu and diamond exhibit no significant anisotropy, so the PDOS of Cu and diamond is the same in different crystal directions. Therefore, the influence of crystal orientation on interfacial thermal transport does not stem from the intrinsic PDOS of Cu and diamond. Through ICMA method and I-PDOS analysis, it can be observed that the crystal orientation-

dependent differences in TBR may be associated with inelastic phonon scattering. Secondly, differences in elastic phonon heat transfer within diamond may also contribute to the variations in TBR.

## Discussion

In this work, an NEP suitable for comprehensive simulation of the interfacial thermal properties in Cu/diamond has been successfully constructed. The effects of interlayer materials, temperature, strain, and crystal orientation on the interfacial thermal transport in Cu/diamond have been studied. Firstly, the method of phonon bridge is proposed to explain the underlying mechanism of the effect of interlayer materials on thermal transport at the Cu/diamond interfaces. When different interlayer materials are used, an increase in the phonon bridge length results in poorer interfacial thermal transport, whereas a decrease in the phonon bridge length leads to improved thermal transport at the interface. When interlayer materials are used, the TBR is also related to the number and matching degree of the interlayer material's efficient phonon channels. The effect of 6 commonly used interlayer materials on the phonon heat transport at the Cu/diamond interface are also analyzed in detail. Secondly, temperature also has a significant impact on interfacial thermal transport at the Cu/diamond interface. The main reason for the decrease in TBR with the increase of temperature is the change in the overlap of the PDOS between Cu and diamond at different temperatures. Then, uniaxial strain can effectively tune the TBR of the Cu/diamond interface. TBR decreases with the increase of compressive strain, while TBR increases with the increase of tensile strain. The main reason for the above phenomenon is the significant difference in hardness between Cu and diamond, which leads to regular changes in the overlap of PDOS and the number of bonds between Cu atoms and C atoms at interface as strain varies. Finally, the effect of crystal orientation on interfacial thermal transport is also explored in detail. Although the thermal conductivity of Cu and diamond exhibits no significant anisotropy, the TBR of the 9 Cu/diamond heterostructures formed by different crystal orientations shows differences. Through ICMA method and I-PDOS analysis, it can be observed that the crystal orientation-dependent differences in TBR may be associated with inelastic phonon scattering. Secondly, differences in elastic phonon heat transfer within diamond may also contribute to the variations in TBR.

In conclusion, our work provides a relatively comprehensive theoretical investigation of interfacial thermal transport in Cu/diamond systems. Particularly, we focused on key influencing factors such as interlayer materials, temperature, strain, and crystal orientation. Insightful strategies are proposed for tuning and improving the thermal properties of Cu and diamond composites. Our study also demonstrates the versatility and applicability of the trained NEP in predicting thermal transport across the Cu/diamond interface, particularly in simulations involving the relatively uncommon presence of interlayer materials. These advancements lay a foundation and pave the way for further investigations into interfacial thermal transport at Cu/diamond interfaces as well as in other structures containing interlayer materials.

## Methods

### Details of machine learning potentials and training set

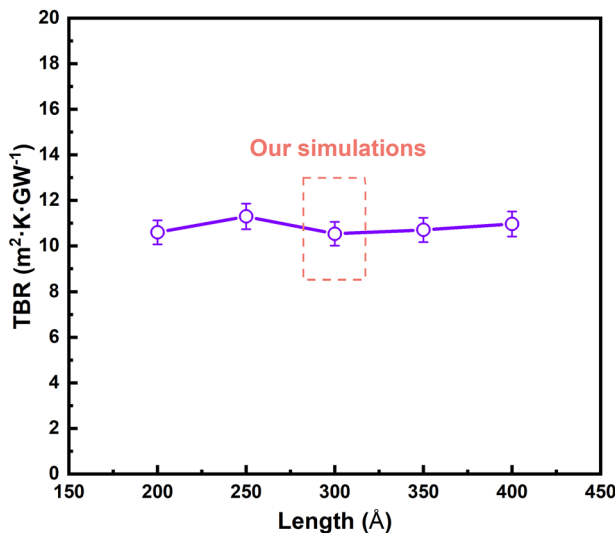
NEP is a neural network (NN) potential that maps the descriptor vector  $q_v^i$  of the central atom  $i$  to its site energy  $U_i$ , the formula can be expressed follows:

$$U_i = \sum_{\mu=1}^{N_{\text{neu}}} \omega_{\mu}^{(1)} \tanh \left( \sum_{v=1}^{N_{\text{des}}} \omega_{\mu v}^{(0)} q_v^i - b_{\mu}^{(0)} \right) - b^{(1)} \quad (1)$$

Detailed information about the above formula can be found in the work published by Song et al.<sup>26</sup>. The NEP model structure consists of three layers: the input layer, the hidden layer, and the output layer. The main logic behind constructing the training data is to provide sufficient and accurate information to the input layer. The training data for this work is obtained from

**Table 1 | Hyperparameters for the NEP training**

| Parameter            | Value | Parameter               | Value             |
|----------------------|-------|-------------------------|-------------------|
| version              | NEP4  | type                    | 6 Cu C Cr Mo Ti W |
| $r_C^R$              | 6 Å   | $r_C^A$                 | 4 Å               |
| $n_{\max}^R$         | 8     | $n_{\max}^A$            | 8                 |
| $N_{\text{basis}}^R$ | 10    | $N_{\text{basis}}^A$    | 10                |
| $l_{\max}^{3b}$      | 4     | $l_{\max}^{4b}$         | 2                 |
| $l_{\max}^{5b}$      | 0     | $N_{\text{neuron}}$     | 50                |
| $N_{\text{batch}}$   | 1200  | $N_{\text{generation}}$ | 300,000           |

**Fig. 9 |** TBR values of Cu(100)/diamond(100) at various model length.**Table 2 | The lattice mismatch for each model**

| Model                | Value |
|----------------------|-------|
| Cu/Cr/diamond        | <1.5% |
| Cu/Mo/diamond        | <1.5% |
| Cu/Ti/diamond        | <1.5% |
| Cu/TiC/diamond       | <2%   |
| Cu/W/diamond         | <1.5% |
| Cu/WC/diamond        | <1.5% |
| Cu/CW/diamond        | <1.5% |
| Cu(100)/diamond(100) | <1%   |
| Cu(100)/diamond(110) | <1.5% |
| Cu(100)/diamond(111) | <1.5% |
| Cu(110)/diamond(100) | <1.5% |
| Cu(110)/diamond(110) | <1%   |
| Cu(110)/diamond(111) | <1.5% |
| Cu(111)/diamond(100) | <1.5% |
| Cu(111)/diamond(110) | <1%   |
| Cu(111)/diamond(111) | <1%   |

the Vienna Ab initio Simulation Package (VASP), based on the DFT method, employing the projected augmented wave (PAW) method and Perdew-Burke-Ernzerhof (PBE) functional<sup>54–57</sup>. A mesh cutoff of 700 eV is used for all structures. The composition of the training data is shown in

Fig. 1a, which mainly includes two parts: single crystal and heterostructure. In order to comprehensively investigate the impact of various factors on the thermal transport at the Cu/diamond interface, 6 common interlayer materials are included in the training data: Cr, Mo, W, Ti, WC, and TiC<sup>13,16,58–60</sup>. The temperature range is set from 200 K to 600 K, and appropriate perturbations and strain are applied to all structures. Finally, 2400 structures are used as training data and 1200 structures are used as test data. In this study, the model structures were constructed using VASPKIT, and the model structures were visualized with the help of OVITO software<sup>61,62</sup>.

The hyperparameters used in training are listed in Table 1. The version used is NEP4, and the potential includes 6 elements: Cu, C, Cr, Mo, Ti, and W.  $r_C^R$  and  $r_C^A$  represent radial cutoff and angular cutoff respectively. The maximum values of the radial and angular descriptor  $n$  indices are  $n_{\max}^R$  and  $n_{\max}^A$  respectively. The number of radial and angular descriptor basis functions is  $N_{\text{basis}}^R$  and  $N_{\text{basis}}^A$  respectively.  $l_{\max}^{3b} = 4$ ,  $l_{\max}^{4b} = 2$  and  $l_{\max}^{5b} = 0$  indicate that three-body action and four-body action are selected and five-body action is not selected.  $N_{\text{neuron}}$  is the number of neurons in the hidden layer of the neural network.  $N_{\text{batch}}$  is the training batch size parameter,  $N_{\text{generation}}$  is the maximum number of iterations, which are set to 1200 and 300,000, respectively. The NEP in this work is particularly applicable to carbon materials whose atomic structures are similar to diamond. For systems with markedly different carbon configurations, the NEP may require fine-tuning with additional training data.

### NEMD simulation

The NEMD method, derived from Fourier's law, is used to explore the heat transfer at the Cu/diamond interface in this work. The heat flux  $J_Q$  in the Cu/diamond system is obtained as:

$$J_Q = \frac{|dQ/dt|}{A} \quad (2)$$

where  $|dQ/dt|$  denotes the energy exchange rate, while  $A$  refers to the area of the simulation box that is perpendicular to the heat flux. According to Fourier's law, thermal boundary resistance TBR is defined as<sup>63</sup>:

$$\text{TBR} = \frac{\Delta T}{J_Q} \quad (3)$$

where  $\Delta T$  represents the temperature difference across the interface region. In order to elucidate the underlying mechanism of the heat transport process, the PDOS is analyzed. PDOS is computed using the Fourier transform of the atomic velocity autocorrelation function, as outlined below<sup>64</sup>:

$$PDOS(\omega) = \int_0^\infty e^{-2\pi i \omega t} \frac{\langle \sum_i v_i(t_0) \cdot v_i(t_0 + t) \rangle}{\langle \sum_i v_i(t_0) \cdot v_i(t_0) \rangle} dt \quad (4)$$

where  $\omega$  is the frequency,  $t_0$  is the start time,  $t$  is correlation time, and  $v_i$  is the velocity vector of the  $i$ -th atom.

During the NEMD simulation, the structure was first fully relaxed via the NPT ensemble, and heat bath was implemented using the NVT ensemble to stabilize the temperature. Subsequently, a temperature gradient was established by applying Langevin thermostat to the heat source and heat sink regions at both ends of the model for 0.5 ns, allowing heat to flow through the system. Thereafter, the temperature distribution was measured during the subsequent 2 ns. Temperature values were collected every 50 ps, and the average of every 50 temperature values was recorded. This process was repeated 80 times, and the final temperature distribution was obtained by averaging the results. To reflect the actual situation, a heat source was placed on the Cu side, and a heat sink was placed on the diamond side, allowing the heat flux to flow from Cu to diamond. After relaxation, the two ends in the z-direction were constrained, and periodic boundary conditions were implemented in the direction with no heat flow. In this work, the model dimensions all exceed  $5 \times 5 \times 30$  nm<sup>3</sup>, containing more than 100,000 atoms

(with slight variations between different models). The results of the model length dependence test on the TBR are shown in Fig. 9, indicating that a length of 30 nm is sufficient to eliminate size effects on the TBR value when Langevin thermostat is applied to the heat source and heat sink regions<sup>65,66</sup>. In all the heterostructures, the lattice mismatch is less than 2%, which is considered an acceptable range in molecular dynamics simulations of interfacial thermal transport<sup>67</sup>. Detailed information is provided in Table 2.

## Data availability

To ensure the reproducibility of the models developed in this study, all datasets will be made publicly available in an open-access repository: <https://github.com/wugai-whu/NEP-Cu-X-diamond-thermal-conductivity.git>.

The more specific explanation and help will be made available upon request.

Received: 23 February 2025; Accepted: 17 October 2025;

Published online: 25 November 2025

## References

1. Moore, A. L. & Shi, L. Emerging challenges and materials for thermal management of electronics. *Mater. Today* **17**, 163–174 (2014).
2. Kang, J. S. et al. Integration of boron arsenide cooling substrates into gallium nitride devices. *Nat. Electron.* **4**, 416–423 (2021).
3. He, Z., Yan, Y. & Zhang, Z. Thermal management and temperature uniformity enhancement of electronic devices by micro heat sinks: A review. *Energy* **216**, 119223 (2021).
4. Xiong, J. et al. Molecular dynamics insights on thermal conductivities of cubic diamond, lonsdaleite and nanotwinned diamond via the machine learned potential. *Chin. Phys. B* **32**, 680–687 (2023).
5. Sun, Z. et al. Investigating thermal transport across the AlN/diamond Interface via the machine learning potential. *Diam. Relat. Mater.* **147**, 111303 (2024).
6. Wu, K. et al. Enhancement of interfacial thermal conductance by introducing carbon vacancy at the Cu/diamond interface. *Carbon* **223**, 119021 (2024).
7. Kanda, S. et al. Fabrication of diamond/Cu direct bonding interface for power device applications. *Jpn. J. Appl. Phys.* **59**, SBBB03 (2019).
8. Jiang, N. et al. Interfacial analysis of CVD diamond on copper substrates. *Diam. Relat. Mater.* **6**, 743–746 (1997).
9. Shi, H. et al. Investigation of heat dissipation and electrical properties of diamond interposer for 2.5-D packagings. *IEEE Trans. Compon., Packaging Manuf. Technol.* **14**, 1601–1609 (2024).
10. Li, M. et al. Binder jetting additive manufacturing of copper/diamond composites: An experimental study. *J. Manuf. Process.* **70**, 205–213 (2021).
11. Peng, J. et al. Fabrication of diamond/copper composite thin plate based on a single-layer close packed diamond particles network for heat dissipation. *Chem. Eng. J.* **476**, 146666 (2023).
12. Xu, B. et al. Scalable monolayer-functionalized nanointerface for thermal conductivity enhancement in copper/diamond composite. *Carbon* **175**, 299–306 (2021).
13. Zhang, Y. et al. Interfacial thermal conductance between Cu and diamond with interconnected W-W<sub>2</sub>C interlayer. *ACS Appl. Mater. Interfaces* **14**, 35215–35228 (2022).
14. Huang, H. et al. Size-and temperature-dependent thermal transport across a Cu-diamond interface: Non-equilibrium molecular dynamics simulations. *Surf. Interfaces* **37**, 102736 (2023).
15. Zhang, C. et al. Microstructure and thermal behavior of diamond/Cu composites: Effects of surface modification. *Diam. Relat. Mater.* **86**, 98–108 (2018).
16. Chang, G. et al. Effect of Ti interlayer on interfacial thermal conductance between Cu and diamond. *Acta Materialia* **160**, 235–246 (2018).
17. Sang, J. et al. Enhanced thermal conductivity of copper/diamond composites by fine-regulating microstructure of interfacial tungsten buffer layer. *J. Alloy. Compd.* **856**, 157440 (2021).
18. Zhou, L. et al. A review of diamond interfacial modification and its effect on the properties of diamond/Cu matrix composites. *Surfaces and Interfaces*, 103143 (2023).
19. Qi, Z. et al. AlN/diamond interface nanoengineering for reducing thermal boundary resistance by molecular dynamics simulations. *Appl. Surf. Sci.* **615**, 156419 (2023).
20. Sun, Z. et al. Insight into interfacial heat transfer of  $\beta$ -Ga<sub>2</sub>O<sub>3</sub>/diamond heterostructures via the machine learning potential. *ACS Appl. Mater. Interfaces* **16**, 31666–31676 (2024).
21. Wu, J. et al. Deep-potential enabled multiscale simulation of gallium nitride devices on boron arsenide cooling substrates. *Nat. Commun.* **15**, 2540 (2024).
22. Sun, Z. et al. Heat transport exploration through the GaN/diamond interfaces using machine learning potential. *Int. J. Heat. Mass Transf.* **241**, 126724 (2025).
23. Qi, Z. et al. Interfacial optimization for AlN/diamond heterostructures via machine learning potential molecular dynamics investigation of the mechanical properties. *ACS Appl. Mater. Interfaces* **16**, 27998–28007 (2024).
24. Sun, Z. et al. A neuroevolution potential for predicting the thermal conductivity of  $\alpha$ ,  $\beta$ , and  $\varepsilon$ -Ga<sub>2</sub>O<sub>3</sub>. *Appl. Phys. Lett.* **123**, 192202 (2023).
25. Zhao, J. et al. Complex Ga<sub>2</sub>O<sub>3</sub> polymorphs explored by accurate and general-purpose machine-learning interatomic potentials. *npj Computational Mater.* **9**, 159 (2023).
26. Song, K. et al. General-purpose machine-learned potential for 16 elemental metals and their alloys. *Nat. Commun.* **15**, 10208 (2024).
27. Sun, Z. et al. Laser stealth dicing of  $\beta$ -Ga<sub>2</sub>O<sub>3</sub>: Theoretical and experimental studies. *J. Mater. Sci. Technol.* 303–312 (2025).
28. Fan, Z., Siro, T. & Harju, A. Accelerated molecular dynamics force evaluation on graphics processing units for thermal conductivity calculations. *Computer Phys. Commun.* **184**, 1414–1425 (2013).
29. Fan, Z., Chen, W., Vierimaa, V. & Harju, A. Efficient molecular dynamics simulations with many-body potentials on graphics processing units. *Computer Phys. Commun.* **218**, 10–16 (2017).
30. Fan, Z. et al. Neuroevolution machine learning potentials: Combining high accuracy and low cost in atomistic simulations and application to heat transport. *Phys. Rev. B* **104**, 104309 (2021).
31. Giri, A. & Hopkins, P. E. A review of experimental and computational advances in thermal boundary conductance and nanoscale thermal transport across solid interfaces. *Adv. Funct. Mater.* **30**, 1903857 (2020).
32. Majumdar, A. & Reddy, P. Role of electron-phonon coupling in thermal conductance of metal-nonmetal interfaces. *Appl. Phys. Lett.* **84**, 4768–4770 (2004).
33. Wu, X. L. Tengfei. Effect of electron-phonon coupling on thermal transport across metal-nonmetal interface —A second look. *Europhys. Lett.* **110**, 67004 (2015).
34. Miao, W. & Wang, M. Importance of electron-phonon coupling in thermal transport in metal/semiconductor multilayer films. *Int. J. Heat. Mass Transf.* **200**, 123538 (2023).
35. Lyeo, H.-K. & Cahill, D. G. Thermal conductance of interfaces between highly dissimilar materials. *Phys. Rev. B* **73**, 144301 (2006).
36. Li, X., Park, W., Chen, Y. P. & Ruan, X. Absence of coupled thermal interfaces in Al<sub>2</sub>O<sub>3</sub>/Ni/Al<sub>2</sub>O<sub>3</sub> sandwich structure. *Appl. Phys. Lett.* **111**, 143102 (2017).
37. Singh, P., Seong, M. & Sinha, S. Detailed consideration of the electron-phonon thermal conductance at metal-dielectric interfaces. *Appl. Phys. Lett.* **102**, 181906 (2013).
38. Giri, A. et al. Mechanisms of nonequilibrium electron-phonon coupling and thermal conductance at interfaces. *J. Appl. Phys.* **117**, 105105 (2015).
39. Hohensee, G. T., Wilson, R. & Cahill, D. G. Thermal conductance of metal-diamond interfaces at high pressure. *Nat. Commun.* **6**, 6578 (2015).

40. Ghosh, S. et al. Dimensional crossover of thermal transport in few-layer graphene. *Nat. Mater.* **9**, 555–558 (2010).

41. Balandin, A. A. Thermal properties of graphene and nanostructured carbon materials. *Nat. Mater.* **10**, 569–581 (2011).

42. Sudhendra, S. et al. Specifics of thermal transport in graphene composites: effect of lateral dimensions of graphene fillers. *ACS Appl. Mater. Interfaces* **13**, 53073–53082 (2021).

43. Sudhendra, S., Kargar, F. & Balandin, A. A. Noncured graphene thermal interface materials for high-power electronics: Minimizing the thermal contact resistance. *Nanomaterials* **11**, 1699 (2021).

44. Sinha, V., Gengler, J. J., Muratore, C. & Spowart, J. E. Effects of disorder state and interfacial layer on thermal transport in copper/diamond system. *J. Appl. Phys.* **117**, 074305 (2015).

45. Gordiz, K. & Henry, A. A formalism for calculating the modal contributions to thermal interface conductance. *N. J. Phys.* **17**, 103002 (2015).

46. Stanley, C. M., Rader, B. K., Laster, B. H., Servati, M. & Estreicher, S. K. The role of interface vibrational modes in thermal boundary resistance. *Phys. Status Solidi (a)* **218**, 2100111 (2021).

47. Sun, B. et al. Vibrational lifetimes and frequency-gap law of hydrogen bending modes in semiconductors. *Phys. Rev. Lett.* **96**, 035501 (2006).

48. Stanley, C. M. Thermal boundary resistance: a review of molecular dynamics simulations and other computational methods. *Phys. Status Solidi (b)* **260**, 2300095 (2023).

49. Nath, P. & Chopra, K. Thermal conductivity of copper films. *Thin Solid Films* **20**, 53–62 (1974).

50. Yu, X. et al. Mechanical regulation to interfacial thermal transport in GaN/diamond heterostructures for thermal switch. *Nanoscale Horiz.* **9**, 1557–1567 (2024).

51. Zhang, R. et al. Modulating electronic properties of  $\beta$ -Ga<sub>2</sub>O<sub>3</sub> by strain engineering. *Results Phys.* **52**, 106916 (2023).

52. Chen, W. et al. Elastic and inelastic phonon scattering effects on thermal conductance across Au/graphene/Au interface. *J. Appl. Phys.* **135**, 165107 (2024).

53. Xu, J. & Guo, Y. Uncovering the roughness effect on inelastic phonon scattering and thermal conductance at interface via spectral energy exchange. *Int. J. Heat. Mass Transf.* **250**, 127295 (2025).

54. Blöchl, P. E. Projector augmented-wave method. *Phys. Rev. B* **50**, 17953 (1994).

55. Kresse, G. & Joubert, D. From ultrasoft pseudopotentials to the projector augmented-wave method. *Phys. Rev. B* **59**, 1758 (1999).

56. Perdew, J. P., Burke, K. & Ernzerhof, M. Generalized gradient approximation made simple. *Phys. Rev. Lett.* **77**, 3865 (1996).

57. Kresse, G. & Furthmüller, J. Efficiency of ab-initio total energy calculations for metals and semiconductors using a plane-wave basis set. *Comput. Mater. Sci.* **6**, 15–50 (1996).

58. Liu, X. et al. Microstructural evolution of sandwiched Cr interlayer in Cu/Cr/diamond subjected to heat treatment. *Thin Solid Films* **736**, 138911 (2021).

59. Chang, G. et al. Mo-interlayer-mediated thermal conductance at Cu/diamond interface measured by time-domain thermoreflectance. *Compos. Part A: Appl. Sci. Manuf.* **135**, 105921 (2020).

60. Chang, G. et al. Regulated interfacial thermal conductance between Cu and diamond by a TiC interlayer for thermal management applications. *ACS Appl. Mater. Interfaces* **11**, 26507–26517 (2019).

61. Wang, V., Xu, N., Liu, J., Tang, G. & Geng, W. VASPKIT: A user-friendly interface facilitating high-throughput computing and analysis using VASP code. *Computer Phys. Commun.* **267**, 108033 (2021).

62. Stukowski, A. Visualization and analysis of atomistic simulation data with OVITO—the Open Visualization Tool. *Model. Simul. Mater. Sci. Eng.* **18**, 015012 (2009).

63. Swartz, E. T. & Pohl, R. O. Thermal boundary resistance. *Rev. Mod. Phys.* **61**, 605 (1989).

64. Dickey, J. & Paskin, A. Computer simulation of the lattice dynamics of solids. *Phys. Rev.* **188**, 1407 (1969).

65. Gordiz, K. & Henry, A. Phonon transport at interfaces between different phases of silicon and germanium. *J. Appl. Phys.* **121**, 025102 (2017).

66. Landry, E. & McGaughey, A. Thermal boundary resistance predictions from molecular dynamics simulations and theoretical calculations. *Phys. Rev. B—Condensed Matter Mater. Phys.* **80**, 165304 (2009).

67. Men, H. & Fan, Z. Atomic ordering in liquid aluminium induced by substrates with misfits. *Comput. Mater. Sci.* **85**, 1–7 (2014).

## Acknowledgements

This work was funded by the National Natural Science Foundation of China (Grant Nos. 92473102, 52202045, 62004141), the Shenzhen Science and Technology Program (Grant No. JCYJ20240813175906008), and the Open Fund of Hubei Key Laboratory of Electronic Manufacturing and Packaging Integration (Wuhan University) (Grant No. EMPI2025007). The numerical calculations in this paper have been done on the supercomputing system in the Supercomputing Center of Wuhan University.

## Author contributions

Z.S. and H.S. contributed equally to this work. Z.S.: Writing - original draft, Methodology, Investigation, Conceptualization. H.S.: Writing - original draft, Methodology, Investigation. Y.Z.: Data curation, Software. R.L.: Writing - review & editing, Formal analysis. X.S.: Investigation, Visualization. Q.W.: Investigation. Z.Q.: Visualization. L.L.: Writing - review & editing. S.L.: Writing - review & editing. W.S.: Writing - review & editing, Investigation, Funding acquisition, Conceptualization. G.W.: Writing - review & editing, Supervision, Project administration, Software, Funding acquisition, Conceptualization. All authors reviewed the manuscript.

## Competing interests

The authors declare no competing interests.

## Additional information

**Correspondence** and requests for materials should be addressed to Wei Shen or Gai Wu.

**Reprints and permissions information** is available at <http://www.nature.com/reprints>

**Publisher's note** Springer Nature remains neutral with regard to jurisdictional claims in published maps and institutional affiliations.

**Open Access** This article is licensed under a Creative Commons Attribution-NonCommercial-NoDerivatives 4.0 International License, which permits any non-commercial use, sharing, distribution and reproduction in any medium or format, as long as you give appropriate credit to the original author(s) and the source, provide a link to the Creative Commons licence, and indicate if you modified the licensed material. You do not have permission under this licence to share adapted material derived from this article or parts of it. The images or other third party material in this article are included in the article's Creative Commons licence, unless indicated otherwise in a credit line to the material. If material is not included in the article's Creative Commons licence and your intended use is not permitted by statutory regulation or exceeds the permitted use, you will need to obtain permission directly from the copyright holder. To view a copy of this licence, visit <http://creativecommons.org/licenses/by-nc-nd/4.0/>.

© The Author(s) 2025